12-2022

Thermal Atomic Layer Etching of MoS_2 Using MoF_6 and H_2O

Jake Soares
Boise State University

Anil U. Mane
Argonne National Laboratory

Devika Choudhury
Argonne National Laboratory

Steven Letourneau
Argonne National Laboratory

Steven M. Hues
Boise State University

See next page for additional authors

https://doi.org/10.1021/acs.chemmater.2c02549

CHEMISTRY OF MATERIALS

pubs.acs.org/cm

Article

Thermal Atomic Layer Etching of MoS_2 Using MoF_6 and H_2O

Jake Soares, Anil U. Mane, Devika Choudhury, Steven Letourneau, Steven M. Hues, Jeffrey W. Elam, and Elton Graugnard*

Cite This: *Chem. Mater.* 2023, 35, 927−936

Read Online

ACCESS | Metrics & More | Article Recommendations | Supporting Information

ABSTRACT: Two-dimensional (2D) layered materials offer unique properties that make them attractive for continued scaling in electronic and optoelectronic device applications. Successful integration of 2D materials into semiconductor manufacturing requires high-volume and high-precision processes for deposition and etching. Several promising large-scale deposition approaches have been reported for a range of 2D materials, but fewer studies have reported removal processes. Thermal atomic layer etching (ALE) is a scalable processing technique that offers precise control over isotropic material removal. In this work, we report a thermal ALE process for molybdenum disulfide (MoS_2). We show that MoF_6 can be used as a fluorination source, which, when combined with alternating exposures of H_2O, etches both amorphous and crystalline MoS_2 films deposited by atomic layer deposition. To characterize the ALE process and understand the etching reaction mechanism, in situ quartz crystal microbalance (QCM), Fourier transform infrared (FTIR), and quadrupole mass spectrometry (QMS) experiments were performed. From temperature-dependent in situ QCM experiments, the mass change per cycle was −5.7 ng/cm^2 at 150 °C and reached −270.6 ng/cm^2 at 300 °C, nearly 50× greater. The temperature dependence followed Arrhenius behavior with an activation energy of 13 ± 1 kcal/mol. At 200 °C, QCM revealed a mass gain following exposure to MoF_6 and a net mass loss after exposure to H_2O. FTIR revealed the consumption of Mo−O species and formation of Mo−F and MoF_x═O species following exposures of MoF_6 and the reverse behavior following H_2O exposures. QMS measurements, combined with thermodynamic calculations, supported the removal of Mo and S through the formation of volatile MoF_2O_2 and H_2S byproducts. The proposed etching mechanism involves a two-stage oxidation of Mo through the ALE half-reactions. Etch rates of 0.5 Å/cycle for amorphous films and 0.2 Å/cycle for annealed films were measured by ex situ ellipsometry, X-ray reflectivity, and transmission electron microscopy. Precisely etching amorphous films and subsequently annealing them yielded crystalline, few-layer MoS_2 thin films. This thermal MoS_2 ALE process provides a new mechanism for fluorination-based ALE and offers a low-temperature approach for integrating amorphous and crystalline 2D MoS_2 films into high-volume device manufacturing with tight thermal budgets.

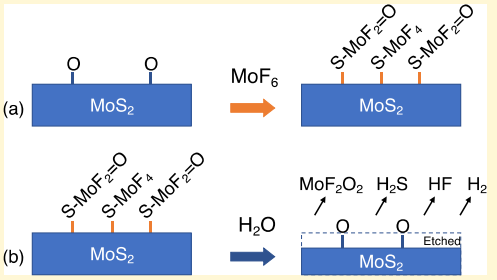

INTRODUCTION

The study of layered transition metal dichalcogenides (TMDs) has been an area of interest due to the potential of integrating these materials into semiconductor manufacturing.[1−3] As monolayers of these materials consist of only a few atoms in thickness and show exceptional performance, they hold promise as replacements for conventional materials such as silicon. Of these materials, molybdenum disulfide (MoS_2) is of great interest[4] due to its thickness of ∼0.65 nm, which is optimal for device scaling,[5] and its tunable band gap, which transitions from the direct to indirect band gaps upon thinning from bulk to monolayer.[6−9] Additionally, amorphous MoS_2 has also shown many promising applications, such as, in hydrogen evolution,[10,11] lithium-ion battery cathodes,[12,13] and photo-detectors.[14]

The integration of TMDs into semiconductor manufacturing requires processes for both deposition and removal within the device's thermal budget constraints. Numerous studies of MoS_2 deposition have been reported, as well as a variety of etching/thinning processes for MoS_2. These include the use of Cl-radicals and Ar^+-ions for step-by-step etching of MoS_2 films,[15,16] CF_4, SF_6, and oxygen plasma-based etching,[17−19] layer thinning by thermal air exposure,[20] and even steam etching.[21] Wang et al. showed the controlled etching of crystalline MoS_2 along the exposed basal planes. It has additionally been shown that defect density from He^+ irradiation within MoS_2 films can be tuned for oxidative etching.[22]

Several of the reported removal processes employ atomic layer etching (ALE), which is a cyclic process that operates by the same principles as atomic layer deposition (ALD) but results in layer-by-layer removal rather than deposition. Plasma-based ALE enables the selective removal of material

Received: August 18, 2022
Revised: December 23, 2022
Published: January 12, 2023

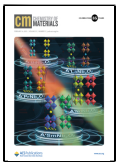

with line-of-sight to the plasma source, while thermal ALE offers isotropic etching of materials with sub-nanometer control, and both hold promise for atomic layer processing of nanoscale device materials.[23,24] Thermal ALE uses self-limiting surface reactions and molecular precursors that modify the surface and create volatile byproducts for removal.[25] This method has been shown to produce low surface defects and has been applied to a variety of material systems. Thermal ALE processes can operate by a few different mechanisms for material removal including fluorination, conversion, oxidation, halogenation, self-limiting surface ligand mechanisms, and heat treatment.[26]

Many studies of thermal ALE have employed fluorination in the surface modification step in ALE using exposures of HF, SF_4, NbF_5, and WF_6.[27−30] These have been used in ALE processes for metals and oxide and nitride compounds.[25] Here, we report a thermal ALE process for a sulfide, MoS_2, using MoF_6 as the fluorination source and H_2O that allows the precise, isotropic removal of both amorphous and crystalline MoS_2 films. In addition to the MoS_2 study reported here, we have previously reported this etching chemistry for TiO_2 and Ta_2O_5 thin films.[31−33] We first characterize the etching process using in situ quartz crystal microbalance (QCM) experiments as a function of temperature on ALD MoS_2 films prepared using alternating exposures of MoF_6 and H_2S.[34,35] Next, we use Gibbs free energy calculations, Fourier transform infrared (FTIR) spectroscopy, and residual gas analysis (RGA) to identify potential mechanisms for the etching reactions. Finally, we measure the etch per cycle using ex situ spectroscopic ellipsometry (SE) and X-ray reflectivity (XRR) measurements and characterize the properties of etched MoS_2 prepared by ALD and mechanical exfoliation using Raman spectroscopy, X-ray photoelectron spectroscopy (XPS), transmission electron microscopy (TEM), and atomic force microscopy (AFM).

EXPERIMENT

MoS_2 Deposition. ALD MoS_2 films were prepared in a custom viscous flow reactor. Process pressure was held constant at ∼1 Torr by flowing 125 sccm of ultra-high purity nitrogen (99.99% Norco) as a carrier gas. MoS_2 ALD and ALE processes followed the typical dosing scheme of $t_1-t_2-t_3-t_4$, where exposure times are in seconds. t_1 and t_2 denote the MoF_6 [molybdenum(VI) fluoride, Fisher Scientific] dose and purge times. t_3 and t_4 denote the H_2S (hydrogen sulfide, 99.5+ %, Millipore Sigma) or H_2O (Nanopure water) dose and purge times for either deposition or etching, respectively. The MoS_2 ALE typically used a timing scheme of 1.0−20.0−2.5−20.0, while the MoS_2 ALD timing scheme was 1.0−15.0−1.5−15.0. The reactant partial pressures during dosing were ∼100 mTorr for MoF_6, ∼400 mTorr for H_2S, and ∼200 mTorr for H_2O. Due to the high pressure of H_2S, a regulator set at 1 psi and a 200 μm orifice were placed on the H_2S delivery line to reduce the pressure.

Coupon substrates for MoS_2 ALD consisted of Si(100) with a native oxide or Si coated with ALD alumina deposited using trimethylaluminum (TMA, Millipore Sigma) and H_2O. Prior to deposition or etching, the substrates were sonicated for 1 min in acetone, then 1 min in ethanol, and rinsed in Nanopure water. Next, the substrates were subjected to a plasma glow discharge for 30 s at a pressure of ∼2 Torr of air to remove any residual hydrocarbons.

Characterization. In situ QCM measurements were performed with an Inficon ALD sensor head and 14 mm, 6 MHz, gold-coated RC-cut quartz sensor crystals rated for 185 °C (Inficon). The back of the sensor crystal was purged with ∼25 sccm N_2 to prevent deposition on the back side. Prior to QCM measurements, the ALD reactor and the QCM sensor were coated using 50−100 cycles of ALD Al_2O_3 to create a passivation layer and provide a consistent starting surface for the subsequent experiments.

In situ RGA was performed during the H_2O exposures of the MoS_2 ALE using a quadrupole mass spectrometer (QMS, XT200, Extorr) operating in the trend mode to identify the gas-phase products of the H_2O half-reaction. To allow time to capture the ALE reaction byproduct signals, the exhaust valve between the ALD chamber and the pump was closed during the H_2O exposure to maintain a constant, static pressure, and the process gases were sampled by the QMS through a leak valve. To differentiate the ALE reaction byproduct signals from background QMS signals, five successive H_2O doses were performed, and the QMS signals were analyzed after the 1st and 5th H_2O dose. The QMS experiments used longer dose times for the MoF_6 and H_2O ALE precursors to ensure saturation across the ALD Al_2O_3-coated Si wafers and HfO_2 ceramic woven cloth (Zircar Zirconia Inc.). Typically, 50 MoS_2 ALD cycles were performed prior to the QMS etching measurements.

In situ FTIR spectroscopy absorption measurements were performed using a Nicolet 6700 FTIR spectrometer (Thermo Scientific) in the transmission mode integrated with a dedicated ALD reactor equipped with IR-transparent KBr windows.[36] The substrate consisted of ZrO_2 nanoparticles (<100 nm diameter, Sigma-Aldrich) pressed into a resistively heated stainless-steel grid with a thickness of 50 μm. Gate valves were closed during the ALD/ALE precursor exposures to protect the KBr windows. The ZrO_2 nanoparticles were first coated with ∼1 nm ALD MoS_2 using 15 cycles of MoF_6 and H_2S at 200 °C. Next, MoS_2 ALE was performed using alternating exposures of MoF_6 and H_2O at 200 °C, and IR spectra were recorded after each precursor exposure in the range of 500−1500 cm^{-1} with a resolution of 4 cm^{-1}. Each spectrum was averaged over 256 scans.

Ex situ SE thickness measurements were made on a J.A. Woollam M-2000 in the spectral range of 250−1680 nm. On each sample, five-point scans were taken at angles of incidence of 60 and 70°, and the reported thickness values represent averages of these multiple measurements. The SE data were fit using CompleteEASE 5.10 (J.A. Woollam) using models of multi-layer film stacks consisting of a Si substrate, a native oxide layer, an Al_2O_3 Cauchy layer, and a MoS_2 film. A B-spline oscillator was used to model the MoS_2 films.[37−39] XRR measurements were acquired with a Bruker D8, and the data were analyzed using Diffrac Plus LEPTOS 6 software version 6.03.

Ex situ Raman spectroscopy was conducted on a Horiba LabRAM system in the reflection mode. A 532 nm excitation laser with a 100× aperture was used to probe samples. A neutral density filter setting ranging from 1 to 10% was used to prevent damage to the MoS_2 samples. Spectra were acquired over the 360−440 cm^{-1} range to capture the crystalline MoS_2 modes.[8]

Ex situ XPS measurements were performed using a Physical Electronics 5600 ESCA system using a monochromated Al Kα source with a spot size of 0.8 mm × 2 mm. Survey scans used a

https://doi.org/10.1021/acs.chemmater.2c02549
Chem. Mater. 2023, 35, 927−936

pass energy of 200 eV and a step size of 1 eV. High-resolution scans used a pass energy of 23 eV and a step size of 0.05 eV. The XPS data were analyzed using MultiPak 9.6. All spectra were referenced to the 1s peak of adventitious carbon (284.8 eV). Peak fitting of all high-resolution scans utilized a Shirley background to define the baseline. Region bounds were chosen such that bounds encompassed the totality of peaks present and were extended as far as possible without overlapping with other chemical peaks nearby. A Gaussian−Lorentz peak mix was used when fitting spectra.

Carbon nanotube (CNT) images were acquired with a LaB_6 JEOL JEM-2100 TEM microscope at 200 keV. Hydroxylated multiwall CNTs (Nanostructured & Amorphous Materials, Inc.) were dispersed in ∼2 mL of ethanol, sonicated for 10 min, and then drop cast onto 400 mesh stainless-steel TEM grids (Ted Pella, Inc.). Roughly 10 nm of ALD alumina was deposited onto CNTs prior to MoS_2 ALD and etching experiments.

AFM measurements were performed on a Dimension FastScan (Bruker) operating in the PeakForce tapping mode. ScanAsyst-air probes (Bruker) with a tip radius of 2 nm were used for imaging. For ALE of exfoliated MoS_2, exfoliated flakes from a bulk MoS_2 crystal were transferred using tape to a Si wafer with a 100 nm thermal oxide. Image processing was carried out in NanoScope Analysis 1.9.

RESULTS AND DISCUSSION

QCM Measurements. In situ QCM measurements were performed to characterize the MoS_2 ALE process. These measurements are facilitated by our ability to deposit ALD MoS_2 on the QCM surface using alternating exposures of MoF_6 and H_2S and then perform MoS_2 ALE using alternating exposures of MoF_6 and H_2O without the need to open the ALD reactor between experiments. Both the MoS_2 ALD and the MoS_2 ALE were monitored using in situ QCM measurements. The mass changes during MoS_2 ALD and subsequent ALE, both at 200 °C, are shown in Figure 1a. The MoS_2 ALD was carried out over 100 cycles, as indicated by the blue arrow, and yielded a linear mass increase versus time. Following a brief pause where the mass was constant, a linear mass loss was observed during 50 cycles of MoS_2 etching, as indicated by the orange arrow. In these experiments, the ALD MoS_2 film is deposited on top of an ALD Al_2O_3 layer. When the mass decrease due to the etching approaches the mass of the initial MoS_2 film, the etch rate decreases toward zero, indicating an "etch stop" (see Figure S1 in the Supporting Information), similar to the etch stop behavior reported previously for Al_2O_3 ALE.[40] The etch stop behavior observed here is attributed to an aluminum fluoride layer that forms during the initial MoS_2 ALD cycles on Al_2O_3 but is not etched by the MoF_6/H_2O chemistry.[35]

Figure 1b plots the mass changes recorded by in situ QCM during two MoS_2 ALE cycles. The average mass gain during the MoF_6 dose was 42 ng/cm^2, and the average mass loss during the H_2O dose is −61 ng/cm^2. The mass change following one complete MoS_2 ALE cycle is −19 ng/cm^2. The structure of the QCM signals in Figure 1b suggests that the MoF_6 exposure modifies the surface such that the subsequent H_2O exposure removes surface material. A mass increase of ∼20 ng/cm^2 is seen during the last few seconds of the H_2O purge step, and we hypothesize this to be a temperature-induced artifact unrelated to the MoS_2 ALE surface chemistry. We note that the RC-quartz sensor has a positive temperature

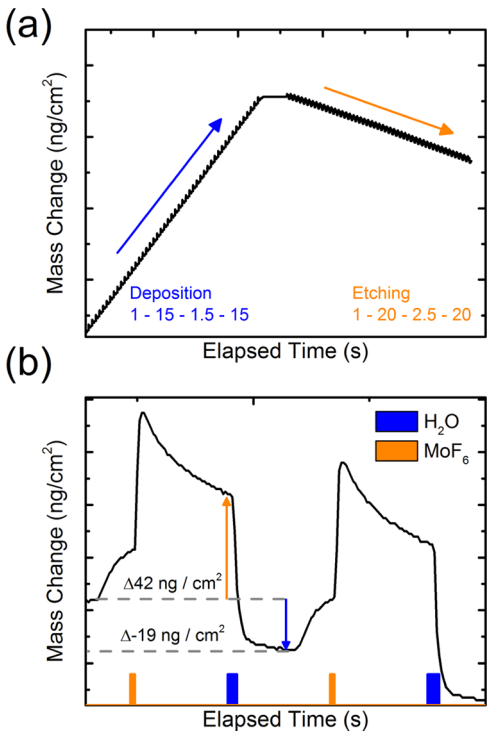

Figure 1. (a) Mass changes observed by in situ QCM during growth and subsequent etching of MoS_2 films on alumina at 200 °C. The blue arrow indicates the region of MoS_2 ALD, and the orange arrow indicates the region of MoS_2 ALE. (b) In situ QCM data during two cycles of MoS_2 ALE. A mass gain of ∼42 ng/cm^2 can be measured after the MoF_6 dose, followed by a net mass loss of 19 ng/cm^2 following the H_2O dose. Orange and blue markers at the bottom of the figure indicate MoF_6 and H_2O doses, respectively.

coefficient at 200 °C.[41] Consequently, the mass increase corresponds to a temperature decrease and may reflect a return to equilibrium following transient heating by the H_2O dose or an exothermic etching reaction.

Experiments with varied precursor doses were performed to establish the saturating dose conditions for both MoF_6 and H_2O. Roughly 5 nm of alumina was deposited on the QCM crystal prior to 50 cycles of MoS_2 ALD at 200 °C. Figure 2a shows the MoS_2 mass loss per ALE cycle versus the MoF_6 pulse time. These measurements used the timing sequence $t_1-t_2-t_3-t_4$, where t_1 denotes the MoF_6 pulse time, which was varied from t_1 = 0.5−3 s with the H_2O pulse time held at t_3 = 3.5 s. The t_2 and t_4 purge times were both held at 20 s. The MoF_6 saturation measurements are well fit using a Langmuir absorption model (black curve) and reveal a saturation time of ∼1 s. Figure 2b shows a similar saturation curve for H_2O, where the MoF_6 pulse was held constant at t_1 = 1 s and the H_2O pulse time varied from t_3 = 0.5−4 s. H_2O also follows a Langmuir absorption model (black curve) and reveals a saturation time of ∼2.5 s. These saturating dose times produced a mass loss of ∼19 ng/cm^2.

To investigate the temperature dependence of the MoS_2 ALE process, QCM measurements were performed during MoS_2 etching at different temperatures, and the data are shown in Figure S2a of the Supporting Information. For each etching temperature, initial MoS_2 films were deposited at 200 °C prior to etching. During the etching process, 20 ALE cycles were conducted to determine the net mass change per cycle (MCPC) versus etching temperature. The MCPC increased

https://doi.org/10.1021/acs.chemmater.2c02549
Chem. Mater. 2023, 35, 927−936

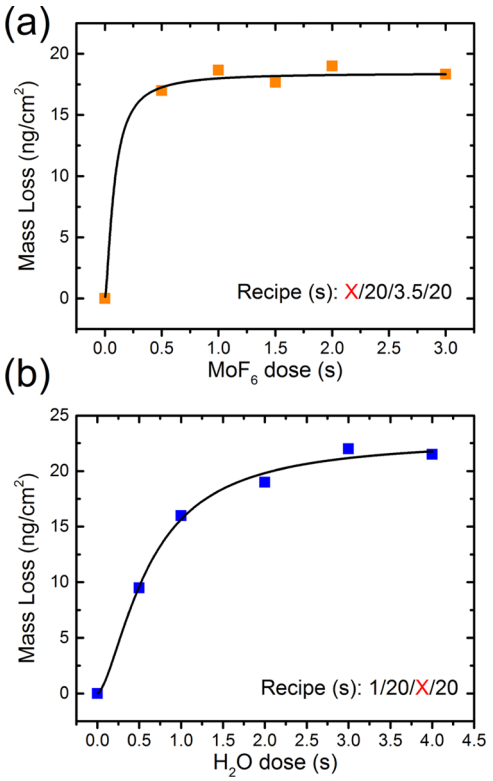

Figure 2. QCM saturation curves for precursors (a) MoF_6 and (b) H_2O during ALE at 200 °C. ALE timing sequence followed X/20/3.5/20 and 1/20/X/20 s for MoF_6 and H_2O, respectively, where X was 0.5, 1.0, 1.5, 2.0, and 3.0 (and 4.0 for H_2O).

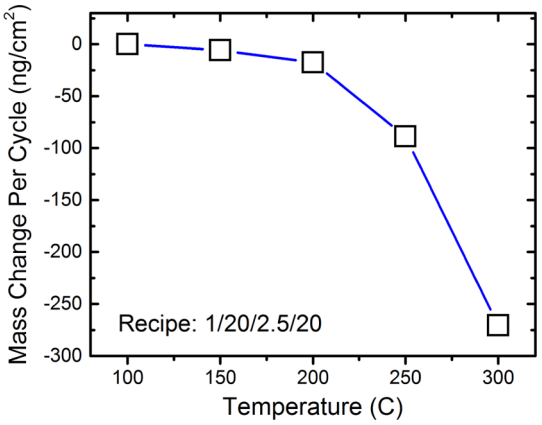

Figure 3. QCM measurements of averaged MCPC between etching temperatures of 100−300 °C using the timing sequence 1−20−2.5−20 s. The mass loss increases dramatically with the etching temperature.

with increasing temperature as can be visualized in Figure 3. The last three cycles during the ALE process were used to average the MCPC at each temperature. No mass change was observed at an etch temperature of 100 °C. When the temperature was increased slightly to 150 °C, a small mass change was observed and calculated to be $MCPC_{150°C} = -5.7$ ng/cm^2. At 200 °C, the calculated $MCPC_{200°C} = -17.5$ ng/cm^2, deviating slightly from the earlier calculated ~19 ng/cm^2. Next, etching at 250 °C showed a much higher mass change of $MCPC_{250°C} = -88.7$ ng/cm^2. Lastly, when the temperature was elevated to 300 °C, the $MCPC_{300°C} = -270.6$ ng/cm^2, an order of magnitude higher than at 200 °C. While these etching results are based on QCM observations for etching an amorphous MoS_2 film, it is interesting to compare these etch rates to the mass equivalent of a crystalline MoS_2 monolayer, which is roughly 307 ng/cm^2. Thus, at 200 °C, the mass equivalent of 6% of a monolayer is etched per cycle, while the mass equivalent of 88% of a monolayer is etched per cycle at 300 °C. These results suggest that higher temperatures help volatilize and remove more material, and an Arrhenius plot of the MCPC data, shown in Figure S2b of the Supporting Information, is consistent with an activated process. For the etching at 300 °C, it was observed that there was mass loss after both the MoF_6 and H_2O pulses. This result suggests the elevated temperature leads to fluorination and subsequent volatilization of residual MoO_x species remaining on the surface following the H_2O pulse. Additionally, reports of MoS_2 etching by thermal annealing and annealing in an O_2/H_2O environment show the primary source of etching was the oxidation of MoS_2, and subsequent volatilization formed MoO_3[20] or $MoO_2(OH)_2$ species.[42] This behavior was observed at temperatures of 330 and 350 °C. For our process, it can be assumed that the higher temperatures and additional thermal energy promote etching during fluorination after the MoF_6 pulse and volatilization of molybdenum oxide/hydroxide species after the H_2O pulse.

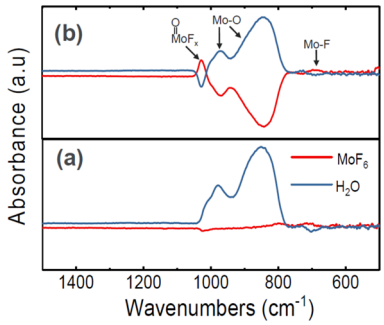

Figure 4. In situ FTIR difference spectra recorded following MoF_6 and H_2O exposures for MoS_2 ALE on an ALD MoS_2 surface during the first (a) and second (b) MoS_2 ALE cycles.

Etching Chemistry. In this section, we propose surface reactions for the MoS_2 ALE based on in situ FTIR spectroscopy and quadrupole mass spectrometry (QMS) measurements and thermodynamic calculations. A general equation for the overall etching chemistry for 1 mole of MoS_2 is

$$MoS_2 + xMoF_6(g) + yH_2O(g) \rightarrow \text{products}(g) \quad (1)$$

where x and y are the moles of MoF_6 and H_2O consumed, respectively, and "products" represent gaseous species containing all the elements on the left side of the equation. This overall equation can be split into separate half-equations describing the chemistry for the individual MoF_6 and H_2O precursor exposure steps. The QCM step shape in Figure 1b provides insights into the relative amounts of gaseous products formed during the MoF_6 and H_2O half-reactions. If we assume that $x = 1$ in eq 1and that all the gaseous products are released during the H_2O half-reaction, then the mass gain during the MoF_6 reaction should be m_1 = mass of MoF_6 = 210 g/mol and the mass loss following one complete cycle should be m_2 = −mass of MoS_2 = −160 g/mol so that the predicted ratio m_2/

https://doi.org/10.1021/acs.chemmater.2c02549
Chem. Mater. 2023, 35, 927−936

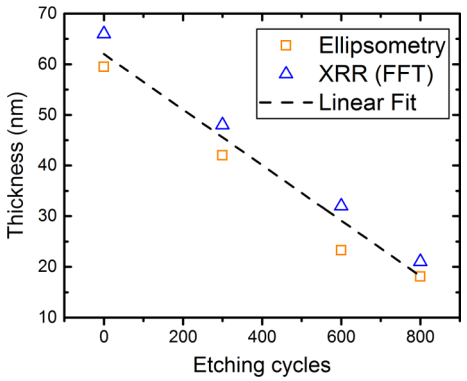

Figure 5. Thickness measurements were acquired after etching of amorphous as-deposited ALD MoS_2 films on SiO_2 coupons at 200 °C. Both SE and XRR thickness measurements show a linear decrease in film thickness. A linear fit of the data produces an etching rate of 0.05 nm/cycle for amorphous MoS_2.

$m_1 = -0.76$. From Figure 1b, the experimental mass ratio is $m_2/m_1 = -0.45$. The smaller experimental mass ratio compared to the predicted mass ratio suggests that all the gaseous products are released during the H_2O half-reaction as assumed, but that $x > 1$, indicating that additional MoF_6 adsorbs during the MoF_6 half-reaction. This MoF_6 may participate in the MoS_2 ALE surface chemistry or may physisorb during the MoF_6 exposure and desorb during the H_2O exposure.

We performed in situ FTIR measurements to identify the surface functional groups formed and consumed during the MoS_2 ALE. For these experiments, we first performed 15 MoS_2 ALD cycles to deposit a MoS_2 thin film on ZrO_2 nanoparticles pressed into the FTIR sample grid. This MoS_2 thin film served as the starting surface for our in situ FTIR investigation of the MoS_2 ALE surface chemistry. The red trace in Figure 4a shows the FTIR spectrum following the first MoF_6 exposure on the MoS_2 surface. In this difference spectrum, the spectrum from the initial ALD MoS_2 on ZrO_2 nanoparticles has been subtracted. Consequently, positive features in this spectrum represent species created by the MoF_6 exposure, and negative features result from consumed species. The only notable feature in this spectrum is a small, positive peak at 690 cm^{-1} that we attribute to the Mo−F stretch.[43] The ZrO_2 nanoparticles absorb significantly in this wavelength region, and this likely reduces the intensity of the Mo−F stretching feature. Following the first H_2O exposure (blue trace in Figure 4a), a small negative feature appears at 690 cm^{-1} indicating the consumption of Mo−F species, and two broad positive features appear at 850 and 975 cm^{-1} that we attribute to Mo−O vibrations.[44,45] Following the second MoF_6 exposure (red trace in Figure 4b), the Mo−O features are consumed, Mo−F features are created, and a new positive feature appears at 1028 cm^{-1} that we attribute to the Mo═O stretch in MoF_xO surface species.[46] The blue trace in Figure 4b shows the difference spectrum following the H_2O exposure in the second ALE cycle and reveals the consumption of Mo−F and MoF_x═O surface species and the creation of Mo−O species.

We next performed in situ QMS measurements to identify the gas phase species of the MoS_2 ALE surface reactions. Section S2 of the Supporting Information presents detailed QMS measurements performed during the H_2O exposure for MoS_2 ALE, and the results indicate that MoF_2O_2 is a viable gaseous byproduct that accounts for Mo removal (Figure S3). The MoF_2O_2 byproduct is similar to WF_2O_2, which was reported to be a gaseous byproduct produced during W etching using WF_6 and O_2 at temperatures of 220−300 °C.[47] Similarly, the in situ QMS measurements suggest that H_2S is the most abundant sulfur-containing byproduct formed during the H_2O exposures (Figure S4). We note that elemental sulfur may form during the MoS_2 ALE reactions and desorb from the surface as $S_8(g)$, but our QMS would not detect this species as it would likely condense before reaching the QMS ionizer. HF and H_2 were also observed by QMS as gaseous byproducts formed during the H_2O exposures (Figure S5).

Table 1 presents three possible overall reactions for the MoS_2 ALE chemistry that produce the gaseous products identified by the in situ QMS measurements, along with the bulk equilibrium free energy values calculated using HSC Chemistry software[48] in units of kJ/mol of MoS_2. While each of these reactions has a negative free energy, indicating thermodynamic favorability, eq 3 has a free energy value nearly five times higher than eq 2 and nearly two times higher than eq 4. In addition, eq 3 is the only reaction showing all of the observed gaseous hydrogen-containing products: H_2S, HF, and H_2. For these reasons, we believe eq 3 is the most likely overall chemical reaction for the MoS_2 ALE, but all three reactions may occur to some extent. It is worth noting that Mo is in the +4 oxidation state in MoS_2 but +6 in the $MoF_2O_2(g)$ product, so the Mo is oxidized in the etching process and the corresponding reduced species would be $H_2(g)$. Supplemental energy calculations (Table S1 of the Supporting Information) show that upon subsequent exposure to MoF_6, any solid molybdenum oxyfluoride/oxide species will form gaseous byproducts, and that the direct reaction of H_2O with MoS_2 is not energetically favorable. This result may be relevant to the QCM observations for etching at 300 °C and the mass loss after the MoF_6 pulse.

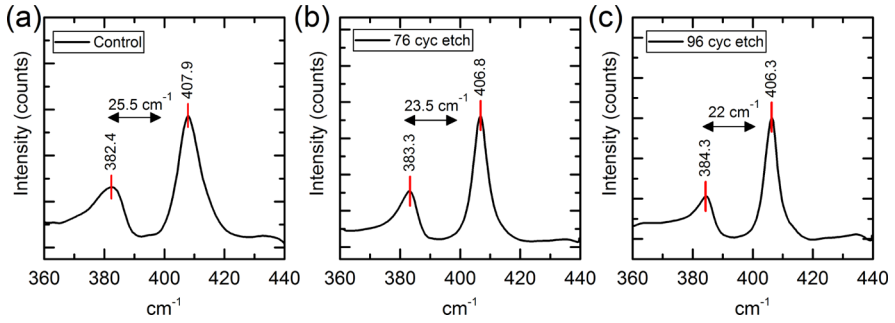

Figure 6. Raman spectra of annealed MoS_2 ALD films after deposition (control) and etching at 200 °C. E^1_{2g} and A_{1g} peak separations indicate (a) a bulk film for un-etched MoS_2, (b) ∼3 layers after 76 ALE cycles, and (c) ∼2 layers after 96 ALE cycles.

https://doi.org/10.1021/acs.chemmater.2c02549
Chem. Mater. 2023, 35, 927−936

Table 1. Gibbs Free Energy Calculations of Etching Reactants and Proposed Etching Products[a]

$$2MoS_2 + MoF_6(g) + 6H_2O(g) \rightarrow 3MoF_2O_2(g) + 4H_2S(g) + 2H_2(g); \quad \Delta G = -40\ \text{kJ/mol} \tag{2}$$

$$MoS_2 + MoF_6(g) + 4H_2O(g) \rightarrow 2MoF_2O_2(g) + 2HF(g) + 2H_2S(g) + H_2(g); \quad \Delta G = -193\ \text{kJ/mol} \tag{3}$$

$$MoS_2 + MoF_6(g) + 4H_2O(g) \rightarrow 2MoF_2O_2(g) + 2HF(g) + 3H_2(g) + 0.25S_8(g); \quad \Delta G = -108\ \text{kJ/mol} \tag{4}$$

[a]Calculations were performed at 200 °C, and values are in kJ/mol of MoS_2.

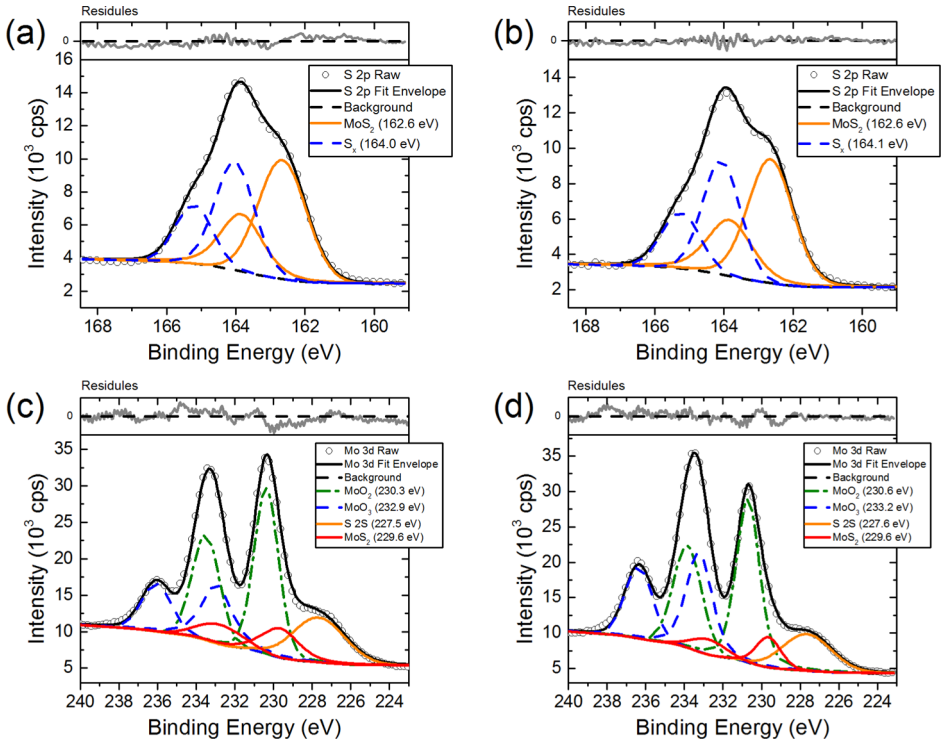

Figure 7. XPS scans of amorphous as-deposited MoS_2 samples before and after etching cycles at 200 °C. High-resolution scans of S 2p and Mo 3d regions before (a,c) and after (b,d) 144 etching cycles. A small increase in MoO_3 peaks is observed, indicating the formation of molyoxide species after the H_2O dose. No apparent differences in spectra indicate the overall lack of alteration of the film after the etching process.

Based on the in situ measurements and thermodynamic calculations, we hypothesize that MoS_2 ALE follows a fluorination and oxygenation mechanism[26] according to the following half-reactions, where surface species are indicated with asterisks

$$S_2Mo - O^* + MoF_6(g) \rightarrow S - MoF_2 = O^* + S - MoF_4^* \tag{5}$$

$$S - MoF_2 = O^* + S - MoF_4^* + 4H_2O(g) \rightarrow O^* + 2MoF_2O_2(g) + 2H_2S(g) + 2HF(g) + H_2(g) \tag{6}$$

In eq 5, MoS_2 with adsorbed oxygen reacts with $MoF_6(g)$ to form S−MoF_2=O* and S−MoF_4*. This reaction consumes Mo−O bonds and forms Mo−F and MoF_x=O in agreement with the in situ FTIR measurements and generates no gaseous products in agreement with the in situ QCM measurements. This reaction is consistent with our calculations that MoF_6 can disassociate on surfaces to form fluorides and oxyfluorides.[35] We hypothesize that Mo is in the +4 oxidation state in S_2Mo−O* and that both species on the right side of eq 5 have Mo in the +5 oxidation state. In eq 6, the H_2O reaction liberates Mo as $MoF_2O_2(g)$ with Mo in the +6 oxidation state, releases S as $H_2S(g)$, and forms HF(g) and $H_2(g)$ in agreement with the in situ QMS measurements. In agreement with the in situ FTIR measurements, the H_2O reaction consumes Mo−F and MoF_x=O surface species and generates Mo−O species in the form of adsorbed oxygen. We note that eqs 5 and 6 sum to the overall etching reaction eq 3. Additional in situ QMS measurements performed during the MoF_6 reaction and in situ XPS measurements to determine the Mo oxidation state could verify these surface reactions.

Etching and Characterization of Films. Ex situ characterization was performed following MoS_2 ALE on ALD MoS_2 films deposited on planar coupons. Initially, 200 MoS_2 ALD cycles were performed at 200 °C on a series of Si coupons. Next, 300−800 MoS_2 ALE cycles were performed using the timing sequence 1/20/2.5/20. After etching, the samples were characterized using SE and XRR measurements to determine the MoS_2 thickness values (SE and XRR data are provided in Section S4 of the Supporting Information). The

https://doi.org/10.1021/acs.chemmater.2c02549
Chem. Mater. 2023, 35, 927−936

XRR thickness values were determined using a fast Fourier transform of the fringes[49] generated by the MoS_2 films. Figure 5 shows the MoS_2 thickness values versus number of MoS_2 ALE cycles from the SE (orange squares) and XRR (blue triangles) measurements. The SE and XRR thickness data were fit by linear regression to yield a value of the −0.50 ± 0.04 Å/cycle.

MoS_2 films were deposited and subsequently etched to test the ability of an etch-back step to produce few-layer crystalline MoS_2 after annealing. A series of Si coupons were first coated with 50 Al_2O_3 ALD cycles, followed by 30 MoS_2 ALD cycles at 200 °C, and the thicknesses were measured by SE to be ∼6.9 nm. Following 96−160 cycles MoS_2 ALE cycles at 200 °C and annealing in H_2S at 650 °C for 30 min to crystallize the MoS_2, the film thicknesses were <7 nm. Raman spectroscopy was performed on all samples after crystallization to investigate crystallinity and to estimate the number of MoS_2 layers. Characteristic E^1_{2g} and A_{1g} modes for MoS_2 were identified in all samples after annealing (Figure 6). The control film that did not undergo etching shows the expected bulk mode separation of $\Delta = 25\ cm^{-1}$ (Figure 6a). This separation has been shown to be constant with thickness for MoS_2 films greater than five layers.[8] The peak-to-peak separation after 76 and 96 etching cycles was found to be $\Delta 76 = 23.5\ cm^{-1}$ (∼3 layers) and $\Delta 96 = 22\ cm^{-1}$, (∼2 layers) respectively (Figure 6b,c).[8] A fourth sample underwent 160 MoS_2 ALE cycles and did not show any characteristic Raman modes, suggesting the MoS_2 film was completely etched away. The Raman data for the 160 cycle MoS_2 ALE sample can be found in Figure S8 in the Supporting Information.

The impact of the thermal ALE process on film morphology was studied by AFM. AFM images were acquired for the amorphous, as-deposited films and after 144 MoS_2 ALE cycles at 200 °C. The surface roughness calculated from the AFM image of the etched film was similar to the roughness for the as-deposited MoS_2 films, with R_a = ∼0.2 nm. AFM height images can be found in Figure S9 of the Supporting Information.

Additional characterization included XPS surface analysis to evaluate the chemical composition of the etched surface. Survey and high-resolution scans of amorphous as-deposited and 144 cycle etched samples were acquired. Low-resolution survey scans can be found in Figure S10 of the Supporting Information. Survey scans of both samples show an elemental composition consistent with previous reports of ALD MoS_2 films prepared using MoF_6 and H_2S.[34] High-resolution scans of the Mo 3d and S 2p regions were obtained to probe if the etching process can lead to differences in surface chemical bonding (Figure 7). These measurements can provide insights into a potential conversion process occurring during ALE. Deconvolution of Mo 3d and S 2p regions shows similar bonding constituents before and after the etching process. A small increase in MoO_3 bonding was observed (roughly ∼10%) and is reflected in Table S2 in the Supporting Information. This small increase in MoO_3 formation suggests molybdenum oxide formation after the H_2O pulse, which is in agreement with the MoS_2 ALE surface chemistry shown in eqs 5 and 6. The overall lack of new peak formation or binding energy shift indicates very little to no alteration of the underlying MoS_2 films during the MoS_2 ALE, where film constituents are again similar to those previously reported for the amorphous as-deposited films.[34]

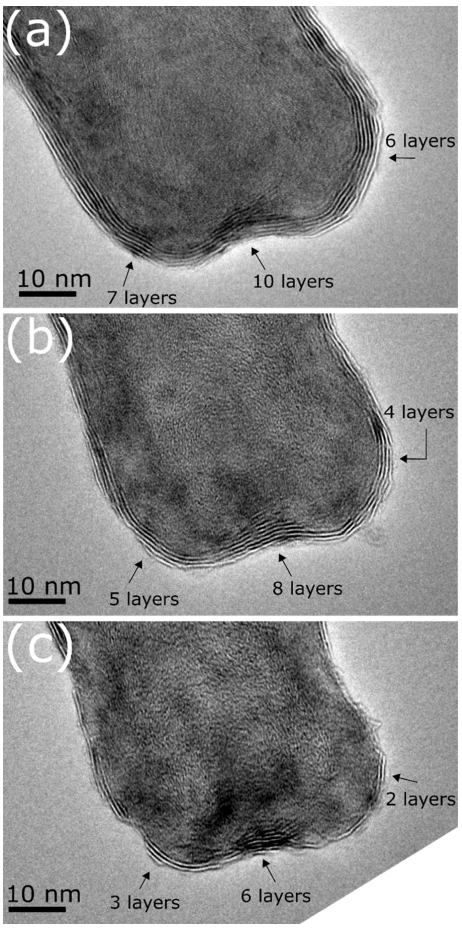

Figure 8. TEM images of MoS_2-coated CNT. (a) Prior to etching, the CNT displayed ∼6−10 layers of MoS_2 as depicted by the arrows. (b) After the first 60 cycles of etching, roughly 2 MoS_2 layers were removed. (c) Additional 60 etching cycles showed the removal of another 2 layers, leaving only 2−6 total MoS_2 layers on the CNT.

Etching of Crystalline MoS_2 Films. We next examined the MoS_2 ALE processes on crystalline MoS_2 films prepared by mechanical exfoliation and MoS_2 ALD. The ALD MoS_2 films were prepared by depositing 35 cycles of MoS_2 on ALD alumina-coated multi-walled CNTs. After the 35 cycles of MoS_2, the CNTs were annealed at 650 °C in H_2S for 30 min to form a crystalline structure.[34,50] MoS_2 flakes were mechanically exfoliated using the scotch tape method and transferred to the thermal oxide Si substrates.

After annealing the MoS_2-coated CNTs, MoS_2 ALE was performed at 250 °C. TEM was performed prior to and after two sets of etching with 60 cycles each, and the TEM images are shown in Figure 8. The MoS_2 region is indicated by the diffraction fringes in Figure 8. Profile line measurements yielded an interlayer spacing of ∼0.7 nm, agreeing well with the literature.[51] Prior to etching, we identified ∼7−10 layers of crystalline MoS_2 encapsulating the alumina-coated CNTs as indicated by the arrows in Figure 8a. After 60 MoS_2 ALE cycles, the thickness was reduced to ∼4−8 layers (Figure 8b). After 120 MoS_2 ALE cycles, the TEM images showed ∼2−5 layers (Figure 8c). In select locations of Figure 8c, the MoS_2 appeared to be completely removed.

These results provide a clear indication of the etching of crystalline ALD MoS_2 films. Based on an MoS_2 thickness of 0.7 nm, an etch rate of roughly 0.02 nm/cycle can be determined.

https://doi.org/10.1021/acs.chemmater.2c02549
Chem. Mater. 2023, 35, 927−936

Alternatively, the etch rate can be estimated as the loss of one MoS_2 layer per 30 ALE cycles. This rate is lower than the etch rate observed for the as-deposited films, as shown in Figure 9. This difference can be attributed to the degree of crystallization of MoS_2, resulting in increased coordination within the material.[50] It has been shown that for several amorphous materials, the etch rate is higher than that of their crystalline counterparts. This result can be observed for the Al_2O_3,[52,53] HfO_2,[54] and ZrO_2[54] systems.

We next studied the effects of MoS_2 ALE on an exfoliated MoS_2 flake. The flake was determined to be bulk MoS_2 from Raman measurements prior to etching. Figure 10a shows an AFM topography scan of the as-prepared exfoliated MoS_2 flake, and Figure 10b,c show AFM topography scans of the same specimen following MoS_2 ALE at 200 and 250 °C, respectively. After the 200 °C etching (Figure 10b), we observe localized topography changes and roughening along the edges of individual layers, similar to grain boundary decoration. In addition, it appears that the central regions of the layers are removed that correspond to defect features on the control image. These results indicate that the MoS_2 ALE initiates at exposed edges and other defect sites at 200 °C, which may allow for defect identification, localization, and chemical modification. The edge sites of the MoS_2 basal planes initiate etching when exposed to steam,[21] and the MoS_2 ALE may follow a similar trend. The topographic differences after etching can be attributed to the formation of MoO_3 species. Walter et al. showed similar results when MoS_2 flakes were exposed to an O_2 heat treatment.[42] They found that longer annealing times (60 min at 500 °C) would ultimately lead to the removal of the MoO_3 particles. To investigate the effect of temperature on the MoS_2 ALE on exfoliated MoS_2, we raised the process temperature to 250 °C and performed an additional 90 MoS_2 ALE cycles. AFM measurements (Figure 10c) showed a reduction in the edge site roughness along the MoS_2 layer perimeters. Besides the initial loss of the smaller crystalline domains, there were no major topographic changes that could be identified on the flake. This result can be attributed to a potentially much slower etch rate as the observed etch rate from amorphous films to the ALD crystalline films dropped significantly. Raman spectroscopy measurements indicate that the as-deposited ALD MoS_2 films are amorphous, whereas the annealed ALD MoS_2 films are ordered. Furthermore, the lack of defects within the exfoliated flake could also prevent available reactive sites for oxidation and subsequent etching,[42,55] again leading to the lack of observed surface changes. We hypothesize that elevated etching temperatures would increase the etch rate on the exfoliated flakes since our QCM data indicated a ~10× etch rate on ALD MoS_2 films at 300 °C compared to 200 °C.

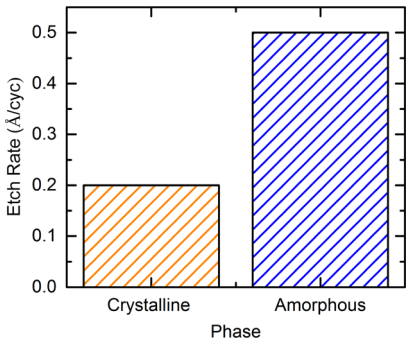

Figure 9. Etch rate dependence on the phase of MoS_2 material. Crystalline MoS_2 etches at a much slower rate compared to amorphous films. Crystalline MoS_2 films etch at the rate of ~0.2 Å/cycle, while amorphous films were observed to etch at the rate of 0.5 Å/cycle.

SUMMARY AND CONCLUSIONS

In this work, we report the thermal ALE of a metal sulfide thin film by etching amorphous and crystalline ALD MoS_2 films and exfoliated MoS_2 flakes using alternating, self-limiting exposures to MoF_6 and H_2O. Based on in situ QCM, FTIR, and QMS measurements and thermodynamic calculations, we propose a mechanism for thermal ALE of MoS_2, in which the MoS_2 surface alternates between oxygenated and fluorinated states in a two-stage oxidation process. The fluorination source, MoF_6, reacts with oxide species on the MoS_2 surface to create surface fluorides and oxyfluorides but releases no gaseous products. The subsequent H_2O exposure removes the Mo and S as volatile MoF_2O_2 and H_2S, respectively, and regenerates the oxygenated MoS_2 surface. The H_2O exposure also generates HF and H_2 gaseous products. In situ temperature-dependent QCM studies revealed a mass loss of −5.7 ng/cm^2/cycle at 150 °C, which increased to −270.6 ng/cm^2/cycle at 300 °C. The temperature-dependent mass changes were consistent with an activated process with a barrier energy of 13 ± 1 kcal/mol. Using ex situ ellipsometry and XRR, amorphous MoS_2 films were found to etch at 0.5 Å/cycle at 200 °C. Etch stop behavior was observed when the etched

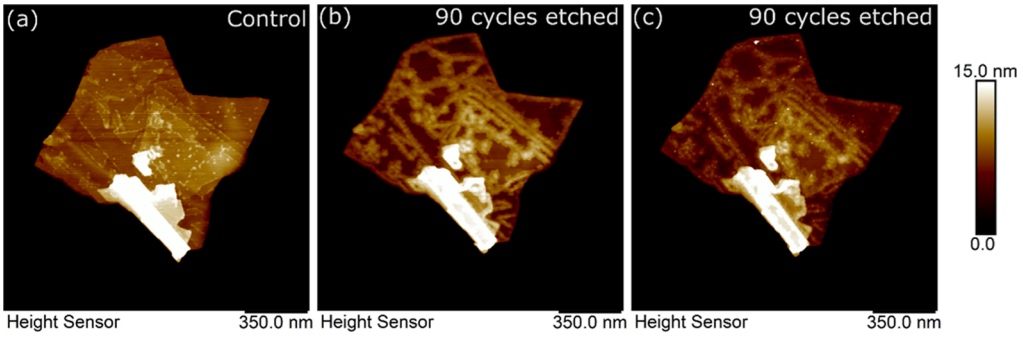

Figure 10. AFM height images of an exfoliated MoS_2 flake on a thermal Si oxide substrate. (a) Exfoliated flake prior to etching. (b) Exfoliated flake following 90 cycles of MoS_2 ALE at 200 °C. (c) Exfoliated flake after an additional 90 cycles of MoS_2 ALE at 250 °C. Initial etching at 200 °C shows roughening of edge sites and removal of small regions across the surface. At 250 °C, roughened edges are removed.

https://doi.org/10.1021/acs.chemmater.2c02549
Chem. Mater. 2023, 35, 927−936

films reached the AlF_3 interface between the ALD MoS_2 film and the underlying ALD alumina layer.

We demonstrated a practical use of our ALE chemistry as a low-temperature process to etch back MoS_2 films on alumina until they neared the MoS_2/alumina interface and, upon annealing, yielded few-layer MoS_2, as supported by Raman spectroscopy measurements. Lastly, we applied the MoS_2 ALE chemistry to crystalline ALD and exfoliated MoS_2 films. The crystalline ALD MoS_2 films etched at ~0.2 Å/cycle at 250 °C. The exfoliated MoS_2 films interestingly showed topographic changes located at the edge sites of the MoS_2 flakes, similar to grain boundary decoration, but no substantial etching was observed. We attribute this behavior to the high degree of crystallinity and low defect density of the exfoliated flakes. This thermal MoS_2 ALE process offers a viable strategy for integrating two-dimensional (2D) MoS_2 films into high-volume manufacturing and may apply to other 2D layered TMDs.

■ ASSOCIATED CONTENT

Supporting Information

The Supporting Information is available free of charge at https://pubs.acs.org/doi/10.1021/acs.chemmater.2c02549.

Data from QCM, QMS, SE, XRR, Raman spectroscopy, AFM, and XPS measurements and additional Gibbs free energy calculations (PDF)

■ AUTHOR INFORMATION

Corresponding Author

Elton Graugnard − *Micron School of Material Science and Engineering, Boise State University, Boise, Idaho 83725, United States; Center for Advanced Energy Studies, Idaho Falls, Idaho 83401, United States;* orcid.org/0000-0002-0497-9821; Email: eltongraugnard@boisestate.edu

Authors

Jake Soares − *Micron School of Material Science and Engineering, Boise State University, Boise, Idaho 83725, United States;* orcid.org/0000-0002-8578-3643

Anil U. Mane − *Applied Materials Division, Argonne National Laboratory, Lemont, Illinois 60439, United States*

Devika Choudhury − *Applied Materials Division, Argonne National Laboratory, Lemont, Illinois 60439, United States*

Steven Letourneau − *Applied Materials Division, Argonne National Laboratory, Lemont, Illinois 60439, United States;* orcid.org/0000-0002-0007-6940

Steven M. Hues − *Micron School of Material Science and Engineering, Boise State University, Boise, Idaho 83725, United States*

Jeffrey W. Elam − *Applied Materials Division, Argonne National Laboratory, Lemont, Illinois 60439, United States;* orcid.org/0000-0002-5861-2996

Complete contact information is available at: https://pubs.acs.org/10.1021/acs.chemmater.2c02549

Author Contributions

All authors have given approval to the final version of the manuscript.

Notes

The authors declare no competing financial interest.

■ ACKNOWLEDGMENTS

We would like to thank members of the Atomic Films Lab for valuable discussions. The work was supported in part by grant no. 1751268 from the National Science Foundation. A portion of this work was supported as part of the Center for Electrochemical Energy Science, an Energy Frontier Research Center funded by the U.S. Department of Energy (DOE), Office of Science, Office of Basic Energy Sciences.

■ REFERENCES

(1) Yun, Q.; Lu, Q.; Zhang, X.; Tan, C.; Zhang, H. Three-Dimensional Architectures Constructed from Transition-Metal Dichalcogenide Nanomaterials for Electrochemical Energy Storage and Conversion. *Angew. Chem., Int. Ed.* **2018**, *57*, 626−646.

(2) Wang, Q. H.; Kalantar-Zadeh, K.; Kis, A.; Coleman, J. N.; Strano, M. S. Electronics and optoelectronics of two-dimensional transition metal dichalcogenides. *Nat. Nanotechnol.* **2012**, *7*, 699−712.

(3) Choi, W.; Choudhary, N.; Han, G. H.; Park, J.; Akinwande, D.; Lee, Y. H. Recent development of two-dimensional transition metal dichalcogenides and their applications. *Mater. Today* **2017**, *20*, 116−130.

(4) Ganatra, R.; Zhang, Q. Few-Layer MoS_2: A Promising Layered Semiconductor. *ACS Nano* **2014**, *8*, 4074−4099.

(5) Liu, H.; Neal, A. T.; Ye, P. D. Channel length scaling of MoS_2 MOSFETs. *ACS Nano* **2012**, *6*, 8563−8569.

(6) Kadantsev, E. S.; Hawrylak, P. Electronic structure of a single MoS_2 monolayer. *Solid State Commun.* **2012**, *152*, 909−913.

(7) Ellis, J. K.; Lucero, M. J.; Scuseria, G. E. The indirect to direct band gap transition in multilayered MoS_2 as predicted by screened hybrid density functional theory. *Appl. Phys. Lett.* **2011**, *99*, 261908.

(8) Li, H.; Zhang, Q.; Yap, C. C. R.; Tay, B. K.; Edwin, T. H. T.; Olivier, A.; Baillargeat, D. From Bulk to Monolayer MoS_2: Evolution of Raman Scattering. *Adv. Funct. Mater.* **2012**, *22*, 1385−1390.

(9) Eda, G.; Yamaguchi, H.; Voiry, D.; Fujita, T.; Chen, M.; Chhowalla, M. Photoluminescence from chemically exfoliated MoS_2. *Nano Lett.* **2011**, *11*, 5111−5116.

(10) Li, G.; Fu, C.; Wu, J.; Rao, J.; Liou, S.-C.; Xu, X.; Shao, B.; Liu, K.; Liu, E.; Kumar, N.; et al. Synergistically creating sulfur vacancies in semimetal-supported amorphous MoS_2 for efficient hydrogen evolution. *Appl. Catal., B* **2019**, *254*, 1−6.

(11) Kwon, Z.; Jin, S.; Shin, W.-S.; Lee, Y.-S.; Min, Y. S. A comprehensive study on atomic layer deposition of molybdenum sulfide for electrochemical hydrogen evolution. *Nanoscale* **2016**, *8*, 7180−7188.

(12) Miki, Y.; Nakazato, D.; Ikuta, H.; Uchida, T.; Wakihara, M. Amorphous MoS_2 as the cathode of lithium secondary batteries. *J. Power Sources* **1995**, *54*, 508−510.

(13) Song, M.; Tan, H.; Li, X.; Tok, A. I. Y.; Liang, P.; Chao, D.; Fan, H. J. Atomic-layer-deposited amorphous MoS_2 for durable and flexible Li−O_2 batteries. *Small Methods* **2020**, *4*, 1900274.

(14) Huang, Z.; Zhang, T.; Liu, J.; Zhang, L.; Jin, Y.; Wang, J.; Jiang, K.; Fan, S.; Li, Q. Amorphous MoS_2 Photodetector with Ultra-Broadband Response. *ACS Appl. Electron. Mater.* **2019**, *1*, 1314−1321.

(15) Kim, K. S.; Kim, K. H.; Nam, Y.; Jeon, J.; Yim, S.; Singh, E.; Lee, J. Y.; Lee, S. J.; Jung, Y. S.; Yeom, G. Y.; Kim, D. W. Atomic layer etching mechanism of MoS_2 for nanodevices. *ACS Appl. Mater. Interfaces* **2017**, *9*, 11967−11976.

(16) Lin, T.; Kang, B.; Jeon, M.; Huffman, C.; Jeon, J.; Lee, S.; Han, W.; Lee, J.; Lee, S.; Yeom, G.; Kim, K. Controlled layer-by-layer etching of MoS_2. *ACS Appl. Mater. Interfaces* **2015**, *7*, 15892−15897.

(17) Jeon, M. H.; Ahn, C.; Kim, H.; Kim, K. N.; LiN, T. Z.; Qin, H.; Kim, Y.; Lee, S.; Kim, T.; Yeom, G. Y. Controlled MoS_2 layer etching using CF_4 plasma. *Nanotechnology* **2015**, *26*, 355706.

(18) Xiao, S.; Xiao, P.; Zhang, X.; Yan, D.; Gu, X.; Qin, F.; Ni, Z.; Han, Z. J.; Ostrikov, K. K. Atomic-layer soft plasma etching of MoS_2. *Sci. Rep.* **2016**, *6*, 19945.

(19) Zhu, H.; Qin, X.; Cheng, L.; Azcatl, A.; Kim, J.; Wallace, R. M. Remote Plasma Oxidation and Atomic Layer Etching of MoS_2. *ACS Appl. Mater. Interfaces* **2016**, *8*, 19119−19126.
(20) Wu, J.; Li, H.; Yin, Z.; Li, H.; Liu, J.; Cao, X.; Zhang, Q.; Zhang, H. Layer thinning and etching of mechanically exfoliated MoS_2 nanosheets by thermal annealing in air. *Small* **2013**, *9*, 3314.
(21) Wang, Z.; Li, Q.; Xu, H.; Dahl-Petersen, C.; Yang, Q.; Cheng, D.; Cao, D.; Besenbacher, F.; Lauritsen, J. V.; Helveg, S.; Dong, M. Controllable etching of MoS_2 basal planes for enhanced hydrogen evolution through the formation of active edge sites. *Nano Energy* **2018**, *49*, 634−643.
(22) Maguire, P.; Jadwiszczak, J.; O'Brien, M.; Keane, D.; Duesberg, G. S.; McEvoy, N.; Zhang, H. Defect-moderated oxidative etching of MoS_2. *J. Appl. Phys.* **2019**, *126*, 164301.
(23) George, S. M.; Lee, Y. Prospects for Thermal Atomic Layer Etching Using Sequential, Self-Limiting Fluorination and Ligand-Exchange Reactions. *ACS Nano* **2016**, *10*, 4889−4894.
(24) Lee, H.-B.-R. The Era of Atomic Crafting. *Chem. Mater.* **2019**, *31*, 1471−1472.
(25) Fischer, A.; Routzahn, A.; George, S. M.; Lill, T. Thermal atomic layer etching: A review. *J. Vac. Sci. Technol., A* **2021**, *39*, 030801.
(26) George, S. M. Mechanisms of thermal atomic layer etching. *Acc. Chem. Res.* **2020**, *53*, 1151−1160.
(27) Lee, Y.; George, S. M. Atomic Layer Etching of Al_2O_3 Using Sequential, Self-Limiting Thermal Reactions with $Sn(acac)_2$ and Hydrogen Fluoride. *ACS Nano* **2015**, *9*, 2061−2070.
(28) Gertsch, J. C.; Cano, A. M.; Bright, V. M.; George, S. M. SF_4 as the Fluorination Reactant for Al_2O_3 and VO_2 Thermal Atomic Layer Etching. *Chem. Mater.* **2019**, *31*, 3624−3635.
(29) Sharma, V.; Elliott, S. D.; Blomberg, T.; Haukka, S.; Givens, M. E.; Tuominen, M.; Ritala, M. Thermal Atomic Layer Etching of Aluminum Oxide (Al_2O_3) Using Sequential Exposures of Niobium Pentafluoride (NbF_5) and Carbon Tetrachloride (CCl_4): A Combined Experimental and Density Functional Theory Study of the Etch Mechanism. *Chem. Mater.* **2021**, *33*, 2883−2893.
(30) Lemaire, P. C.; Parsons, G. N. Thermal Selective Vapor Etching of TiO_2: Chemical Vapor Etching via WF_6 and Self-Limiting Atomic Layer Etching Using WF_6 and BCl_3. *Chem. Mater.* **2017**, *29*, 6653−6665.
(31) Mane, A.; Elam, J.Controlled Layer-by-Layer Etching of ALD Grown Ta_2O_5 Thin Films. *AVS 17th International Conference on Atomic Layer Deposition*: Denver, CO, 2017.
(32) Mane, A. U.; Letourneau, S.; Choudhury, D.; Elam, J. W.ALD and ALEt of Transition Metal Dichalcogenide Materials. *236th ECS Meeting*: Atlanta, GA, 2019.
(33) Mane, A.; Young, M.; Choudhury, D.; Letourneau, S.; Yanguas-Gil, A.; Elam, J.Novel Chemistries for Layer-by-Layer Etching of 2D Semiconductor Coatings and Organic-Inorganic Hybrid Materials. *AVS 20th International Conference on Atomic Layer Deposition*, 2020.
(34) Mane, A. U.; Letourneau, S.; Mandia, D. J.; Liu, J.; Libera, J. A.; Lei, Y.; Peng, Q.; Graugnard, E.; Elam, J. W. Atomic layer deposition of molybdenum disulfide films using MoF_6 and H_2S. *J. Vac. Sci. Technol., A* **2018**, *36*, 01A125.
(35) Soares, J.; Letourneau, S.; Lawson, M.; Mane, A. U.; Lu, Y.; Wu, Y. Q.; Hues, S. M.; Li, L.; Elam, J. W.; Graugnard, E. Nucleation and growth of molybdenum disulfide grown by thermal atomic layer deposition on metal oxides. *J. Vac. Sci. Technol., A* **2022**, *40*, 062202.
(36) Comstock, D. J.; Elam, J. W. Atomic layer deposition of Ga_2O_3 films using trimethylgallium and ozone. *Chem. Mater.* **2012**, *24*, 4011−4018.
(37) Mahlouji, R.; Verheijen, M. A.; Zhang, Y.; Hofmann, J. P.; Kessels, W. M.; Bol, A. A. Thickness and Morphology Dependent Electrical Properties of ALD-Synthesized MoS_2 FETs. *Adv. Electron. Mater.* **2022**, *8*, 2100781.
(38) Su, W.; Wang, Y.; Chen, F.; Fu, L.; Ding, S.; Zhao, S.; Zhang, Q.; Song, K.; Shu, H.; Ma, X. Total absorption of WO_3/WS_2 stacked thin films in middle infrared light. *Infrared Phys. Technol.* **2019**, *103*, 103098.
(39) Chen, X.; Park, Y. J.; Das, T.; Jang, H.; Lee, J.-B.; Ahn, J.-H. Lithography-free plasma-induced patterned growth of MoS_2 and its heterojunction with graphene. *Nanoscale* **2016**, *8*, 15181−15188.
(40) Zywotko, D. R.; Zandi, O.; Faguet, J.; Abel, P. R.; George, S. M. ZrO_2 Monolayer as a Removable Etch Stop Layer for Thermal Al_2O_3 Atomic Layer Etching Using Hydrogen Fluoride and Trimethylaluminum. *Chem. Mater.* **2020**, *32*, 10055−10065.
(41) Riha, S. C.; Libera, J. A.; Elam, J. W.; Martinson, A. B. F. Design and implementation of an integral wall-mounted quartz crystal microbalance for atomic layer deposition. *Rev. Sci. Instrum.* **2012**, *83*, 094101.
(42) Walter, T. N.; Kwok, F.; Simchi, H.; Aldosari, H. M.; Mohney, S. E. Oxidation and oxidative vapor-phase etching of few-layer MoS_2. *J. Vac. Sci. Technol., B* **2017**, *35*, 021203.
(43) Stene, R. E.; Scheibe, B.; Pietzonka, C.; Karttunen, A. J.; Petry, W.; Kraus, F. MoF_5 revisited. A comprehensive study of MoF_5. *J. Fluorine Chem.* **2018**, *211*, 171−179.
(44) Nanayakkara, C. E.; Vega, A.; Liu, G.; Dezelah, C. L.; Kanjolia, R. K.; Chabal, Y. J. Role of Initial Precursor Chemisorption on Incubation Delay for Molybdenum Oxide Atomic Layer Deposition. *Chem. Mater.* **2016**, *28*, 8591−8597.
(45) Hirata, T. In situ observation of Mo-O stretching vibrations during the reduction of MoO_3 with hydrogen by diffuse reflectance FTIR spectroscopy. *Appl. Surf. Sci.* **1989**, *40*, 179−181.
(46) Alexander, L. E.; Beattie, I. R.; Bukovszky, A.; Jones, P. J.; Marsden, C. J.; Schalkwyk, G. J. V. Vapour density and vibrational spectra of $MoOF_4$ and WOF_4. The structure of crystalline WOF_4. *J. Chem. Soc., Dalton Trans.* **1974**, *1*, 81−84.
(47) Xie, W.; Lemaire, P. C.; Parsons, G. N. Thermally Driven Self-Limiting Atomic Layer Etching of Metallic Tungsten Using WF_6 and O_2. *ACS Appl. Mater. Interfaces* **2018**, *10*, 9147−9154.
(48) Smith, W. R. HSC chemistry for Windows, 2.0. *J. Chem. Inf. Comput. Sci.* **1996**, *36*, 151−152.
(49) Lammel, M.; Geishendorf, K.; Choffel, M. A.; Hamann, D. M.; Johnson, D. C.; Nielsch, K.; Thomas, A. Fast Fourier transform and multi-Gaussian fitting of XRR data to determine the thickness of ALD grown thin films within the initial growth regime. *Appl. Phys. Lett.* **2020**, *117*, 213106.
(50) Letourneau, S.; Young, M. J.; Bedford, N. M.; Ren, Y.; Yanguas-Gil, A.; Mane, A. U.; Elam, J. W.; Graugnard, E. Structural evolution of molybdenum disulfide prepared by atomic layer deposition for realization of large scale films in microelectronic applications. *ACS Appl. Nano Mater.* **2018**, *1*, 4028−4037.
(51) Moser, J.; Liao, H.; Levy, F. Texture characterisation of sputtered MoS2thin films by cross-sectional TEM analysis. *J. Phys. D: Appl. Phys.* **1990**, *23*, 624.
(52) Dongzhu, X.; Dezhang, Z.; Haochang, P.; Hongjie, X.; Zongxin, R. Enhanced etching of sapphire damaged by ion implantation. *J. Phys. D: Appl. Phys.* **1998**, *31*, 1647.
(53) Murdzek, J. A.; Rajashekhar, A.; Makala, R. S.; George, S. M. Thermal atomic layer etching of amorphous and crystalline Al_2O_3 films. *J. Vac. Sci. Technol., A* **2021**, *39*, 042602.
(54) Murdzek, J. A.; George, S. M. Effect of crystallinity on thermal atomic layer etching of hafnium oxide, zirconium oxide, and hafnium zirconium oxide. *J. Vac. Sci. Technol., A* **2020**, *38*, 022608.
(55) Kc, S.; Longo, R. C.; Wallace, R. M.; Cho, K. Surface oxidation energetics and kinetics on MoS_2 monolayer. *J. Appl. Phys.* **2015**, *117*, 135301.